CFD Predictions of Soot & *CO* Emissions Generated by a Partially-Fueled 9-Element Lean-Direct Injection Combustor

M.S. Raju
Vantage Partners LLC (NASA GRC GESS-3)
3000 Aerospace Parkway
Brook Park, Ohio-44132

C.T. Wey
NASA Glenn Research Center
21000 Brook Park Road
Cleveland, Ohio-44135

ABSTRACT

A study was undertaken to investigate the CO & soot emissions generated by a partially-fueled 9-element LDI (Lean-Direct Injection) combustor configuration operating in the idle range of jet engine conditions. In order to perform the CFD analysis, several existing soot/chemistry models were implemented into the OpenNCC (Open National Combustion Code). The calculations were based on a Reynolds-Averaged Navier Stokes (RANS) simulation with standard $k-\epsilon$ turbulence model, a 62-species jet-a/air chemistry, a 2-equation soot model, & a Lagrangian spray solver. A separate transport equation was solved for all individual species involved in jet-a/air combustion. In the test LDI configuration we examined, only five of the nine injectors were fueled with the major pilot injector operating at an equivalence ratio (Φ) of near one and the other four main injectors operating at a Φ near 0.55. The calculations helped to identify several reasons behind the soot & *CO* formation in different regions of the combustor. The predicted results were compared with the reported experimental data on soot mass concentration (SMC) & emissions index of CO (EICO). The experimental results showed that an increase in either T_3 and/or F/A ratio lead to a reduction in both EICO & SMC. The predicted results were found to be in reasonable agreement. However, the predicted EICO differed substantially in one test condition associated with higher F/A ratio.

1. INTRODUCTION

One of the major driving factors behind the LDI combustor design effort at NASA GRC is the need to meet various performance & emissions targets set for next-generation combustor development [1]. The LDI design promotes low NOx formation by ensuring most of the combustion to take place in several small lean-burning zones [1]. Numerous experimental & CFD studies were undertaken to document its feasibility over a wide range of combustor operating conditions [1 & 2]. This has lead to the development of several successive generation of LDI, LDI-1, & LDI-2 injector configurations [2]. The experimental studies documented the aerodynamic and combustion behavior of several LDI configurations, the measurements of NOx, CO, & and etc [3, 4 & 16]. Several CFD studies were undertaken to evaluate engine designs based on the LDI concept [2, 5 & 6]. They included results from both single and multi-element LDI injectors based on RANS (Reynolds averaged Navier Stokes) [2], URANS (unsteady RANS) [5 & 6], very large eddy simulation based on TFNS (Time Filtered Navier Stokes) [5], & the combined Monte-Carlo PDF/spray/CFD approach [7 & 15]. More importantly, the CFD studies of Ajmani et al [2] played a major role in the development effort of the last two generation of LDI-1 and LDI-2 arrays.

While considerable effort was undertaken to study NOx emissions [2], one aspect that has not received much attention is the CFD analysis of soot & CO emissions by LDI combustors. It is a subject that needs investigation particularly in the idle range

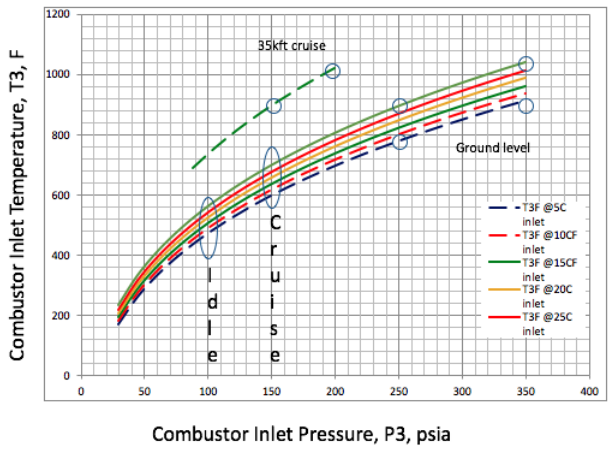

Fig. 1 Combustor operating conditions (courtesy of Lobo et al [2017], NASA GRC).

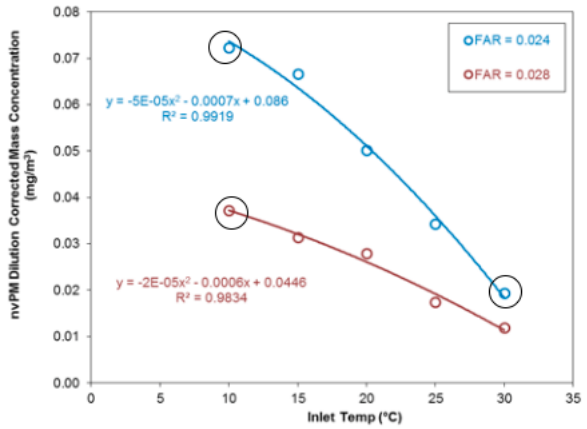

Fig. 2 Soot mass concentration versus inlet temperature variation (courtesy of Lobo et al [2017], NASA GRC).

of engine operating conditions where the LDI injectors are partially fueled. Any inefficient & incomplete combustion resulting from such operating conditions could lead to the formation of soot & CO emissions. Aside from the engineering concerns, soot and its precursors are suspected to be carcinogenic and there is a growing concern on the impact of both soot and CO on climate modifications [8]. In order to address various environmental & engineering concerns, NASA GRC has undertaken a road map for studies on soot and CO emissions generated by LDI combustors as a part of several aeronautics project initiatives [9].

As a part of this effort, we incorporated several soot/chemistry models into OpenNCC. More details of the numerical approach employed in our current calculations can be found in Sec. 3. For validation purposes, we made use of the experimental data reported by Lobo et al [10]. More details of the test data and engine operating conditions can be found in Sec. 2. The LDI array layout and burner geometry used in our computations is described in Sec. 4. In this paper, we describe our computational experience based on the 2-equation soot models of [11] & [12], the gas-phase chemistry based on the 62-species skeletal mechanism of Lu et al [13], & the experimental data of [10].

2. ENGINE OPERATING & EXPERIMENTAL TEST CONDITIONS

The variation of the combustor inlet pressure, P_3, vs combustor inlet temperature, T_3, over the entire range of engine operating conditions is shown in Fig. 1. It is taken from Lobo et al [10]. For our purpose, we selected the test conditions from the idle operating range. Lobo et al [10] reported the experimental data on soot and CO emissions in the form of EICO & SCM. The variation of their reported NvPM dilution corrected mass concentration vs inlet temperature is shown in Fig. 2, & the corresponding variation of EICO vs inlet temperature in Fig. 3. Their data was taken at two distinct fuel/air ratios (FARs). The reported measurements represent the average of data collected over several probes located at multiple locations of the 150mm downstream-plane of the combustor. The observed improvement in both soot and CO emissions due to an increase in either inlet temperature or fuel/air ratio could be attributed to improved combustion.

3. NUMERICAL APPROACH

In an effort to guide in the design and testing of advanced gas-turbine combustors, NASA Glenn research center (GRC) has undertaken the development of OpenNCC. It is developed with the aim of advancing the current multi-dimensional computational tools used in the design of aircraft combustors. Since its inception about 20 years ago, the code has gone though considerable evolution to accommodate the changing needs of various ongoing projects associated with next-generation combustor technology development. More on the current status of OpenNCC can be found in Ref. [5-7 & 14-15]. It can be used in the investigation of both steady/unsteady, reacting/non-

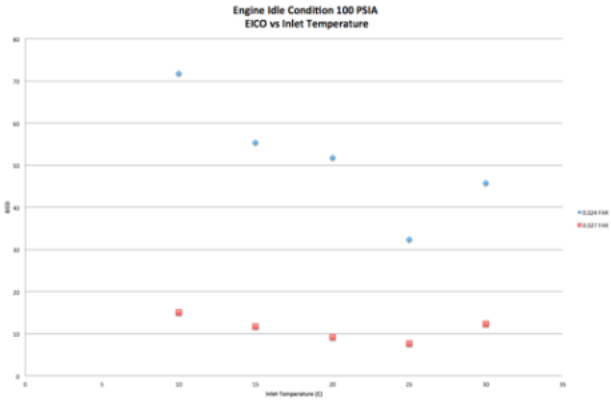

Fig. 3 EICO versus inlet temperature variation (courtesy of Lobo et al [2017], NASA GRC).

reacting, & gaseous/spray calculations by employing a wide variety of turbulence/chemical-kinetic/spray models & different numerical schemes.

3.1 Gas-Phase CFD

Our present computations are based on a RANS (Reynolds-Averaged Navier-Stokes) solution with standard two-equation turbulence model. They are based on a central-differencing scheme with second-order accurate discretization for both viscous and inviscid fluxes. It makes use of a Jameson operator based on a blend of second and fourth-order artificial dissipation terms to achieve numerical stability. The steady-state RANS solution is obtained by making use of an explicit, four-stage Runge-Kutta scheme. The convergence to steady-state is accelerated by making use of residual smoothing of residuals in pseudo time.

3.2 Soot & Emissions Modeling

In a preliminary effort to extend our current capabilities to particulate emissions, we incorporated the 2-equation soot models of both Fairweather et al [11] & Liu et al [12] into OpenNCC [9]. As a part of this effort, we undertook a validation study based on a well-characterized, confined, swirl-induced sooting flame generated by a model aero-engine combustor developed at DLR, Germany [8]. Further details of this investigation can be found in [9].

For the jet-a/air chemistry, our computations are based on the 62-species skeletal mechanism (code-named RED62) developed by T. Lu & co-workers at University of Connecticut. It was developed under a NRA award granted by the NASA TTT (Transformational Tools & Technologies) project office. It includes several steps deemed necessary in the formation of several intermediate species needed in our soot calculations.

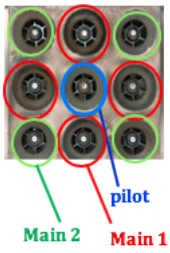

Fig. 4 Layout of the 9-point LDI (courtesy of Lobo et al [2017], NASA GRC).

3.3 Spray Modeling

The liquid-phase computations were performed by making use of LSPRAY-V, the spray module developed as a part of the NCC code development [14]. The spray modeling approach is designed to predict the flow, thermal, and transport properties of a rapidly evaporating multi-component liquid spray based on the dilute spray approximation. It is applicable over a wide range of evaporating conditions (normal, superheat, and supercritical). It also incorporates several well-established atomization, vaporization and wall/droplet impingement models. Its use has been demonstrated in the numerical investigation of various reacting/non-reacting flows encountered in gas-turbine combustors, stratified-charge rotary combustion (Wankel) engines, supersonic and pulse detonation combustion devices [14].

4. THE LAYOUT OF 9-POINT LDI & BURNER GEOMETRY USED IN OUR COMPUTATIONS

The layout of the 9-point LDI used in the computations is shown in Fig. 4. It comprises of Woodward Simplex fuel nozzles (six 60^0 axial swirler-vane air passages and a fuel nozzle). The pilot injector is located in the middle and runs at an equivalence ratio of close to one. The four corner main injectors are not fueled. The remaining main injectors run at an equivalence ratio of less than one. For this injector configuration, the overall AC_D = 1.3 in^2 and FN_{US} = 2.9. The computational geometry of the overall

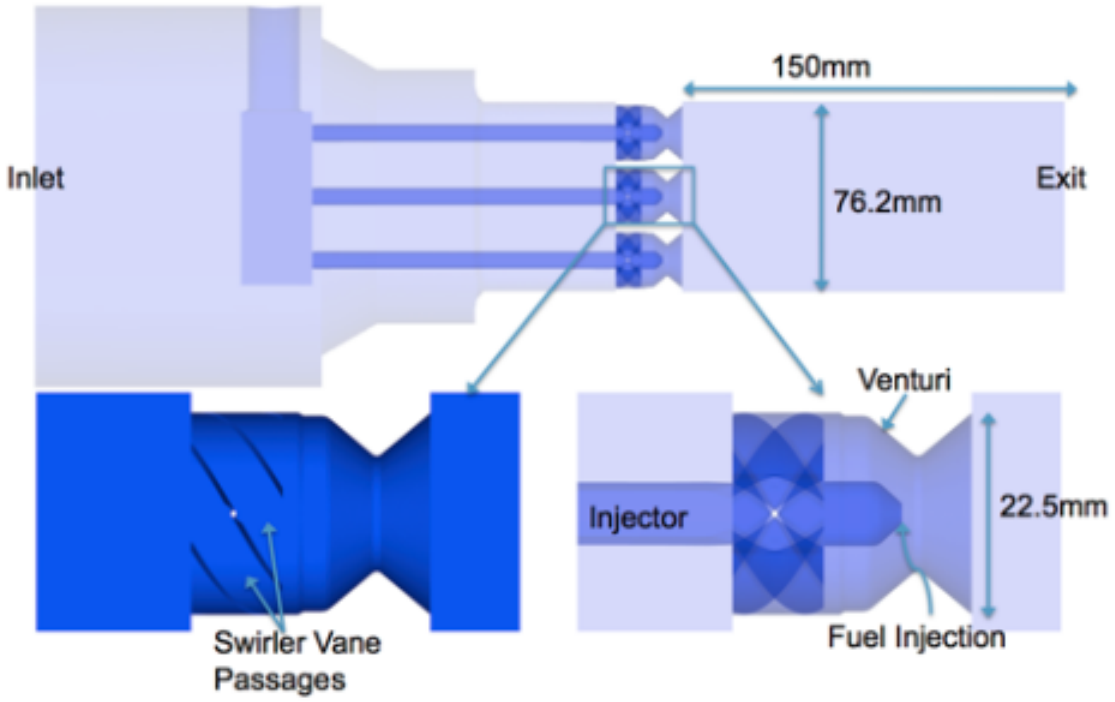

Fig. 5 Geometry of the 9-point LDI (top) and an enlarged view of a single-injection element (bottom) (courtesy of Kumud Ajmani, NASA GRC).

burner configuration used in our calculations is shown in Fig. 5. Also, shown are the enlarged views of a single injector element. The layout provides a good understanding of how the 9-point LDI is embedded inside of the burner geometry. The injector element is placed upstream of an converging-diverging venturi, and it comprises of an air-swirler and an injector assembly. The six axial 60^0 swirler-vanes located on the periphery generate the needed swirl to enable rapid liquid break-up. More importantly, the spray is generated by a centrally-located pressure-swirl atomizer located near the throat of the venturi. Downstream of the venturi, combustion takes place in a square duct that is 150mm long with a cross-section of 76.2mm.

The grid used in our computations was provided by Kumud Ajmani at NASA GRC. More details on the computational grid can be found in [2]. It comprises of about 9.5 million tetrahedral elements. It satisfied the following criteria: (1) it ensured that the pressure drop be calculated within a 10% of the experimental value, (2) it ensured that proper pressure drop be maintained across all the swirl vane-passages by providing sufficient grid clustering upstream of the swirler, and by providing sufficient and yet uniform grid spacing along each of the swirl air-passages, and (3) close attention was paid to the grid clustering and stretching in the combustion region in order to properly resolve several important regions of wall boundary layer and shear-layer [2].

5. INITIAL TEST CONDITIONS USED IN OUR COMPUTATIONS

For the test engine configuration we studied, Lobo et al [10] reported the soot & CO measurements valid over a wide range of idle combustor operating conditions. As described earlier, their measured data can be found in Figs. 2 & 3. For our validation purposes, we selected three test conditions as identified by the largest black-circle symbols in Fig. 2. These conditions were selected primarily to examine the changes in soot and CO emissions resulting from the variations in T_3 and FAR. The resulting overall Φ varies from 0.34 to 0.40, and Φ from 0.9 to 1.09 for the pilot injector & 0.55 to 0.64 for the main injectors. Also, there are slight variations in P_3 from 7.4 to 7.8 bar.

6. RESULTS & DISCUSSION

Table 1. Experimental test conditions.

Calculations	(1)	(2)	(3)
FAR	0.024	0.024	0.028
Inlet T (deg. C)	10	30	10
P_3 (bar)	7.446	7.053	7.791
T_3 (deg. K)	525.373	568.706	525.928
ρ_3 (Kg/m^3)	4.966	4.3128	5.1905
air mass flow rate (kg/s)	0.3528	0.34473	0.3538
fuel mass flow rate (kg/s)	0.00849	0.00827	0.009906
Pilot injector equivalence ratio	0.97	0.9	1.09
Main injector equivalance ratio	0.55	0.55	0.64
Overall fuel equivalence ratio	0.34	0.35	0.40

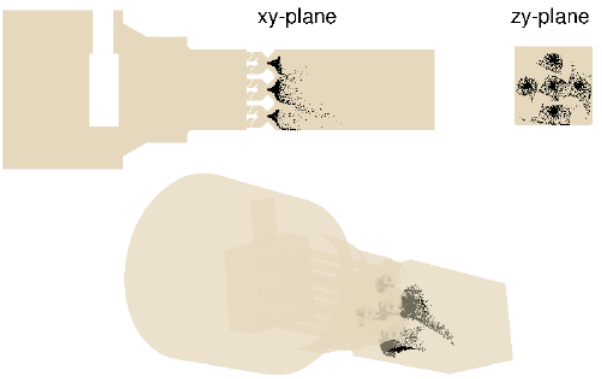

Fig. 7 A 3D perspective & some Sectional views of spray droplet distribution (FAR = 0.024 & T_3 = 569 deg. K).

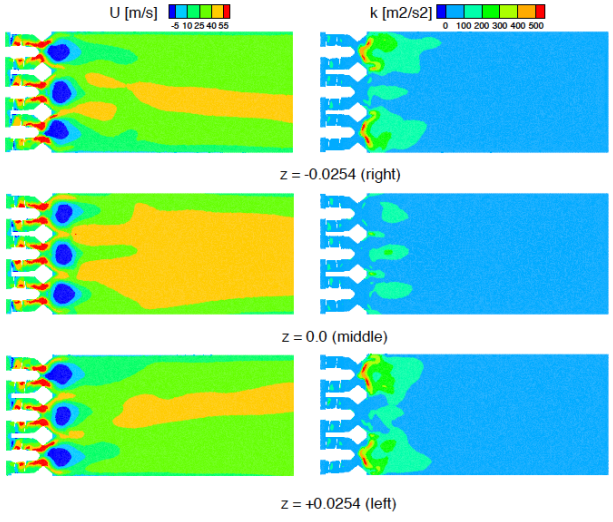

Fig. 6 Sectional views of axial velocity and turbulence kinetic energy (FAR = 0.024 & T_3 = 569 deg. K).

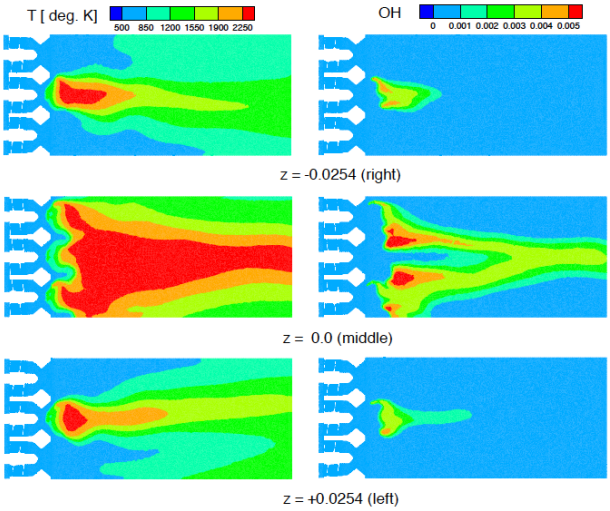

Fig. 8 Sectional views of temperature and OH mass fraction (FAR = 0.024 & T_3 = 569 deg. K).

Since the test conditions are drawn from a narrow range of idle operating conditions, the mean velocity and temperature behavior is expected to be mostly similar. For this reason, we first describe the behavior of the flow-field in some considerable detail based on the predicted results obtained from the second test condition. It will be followed by a discussion of the differences/similarities observed between different test conditions. Finally, the comparisons between the predicted and measured results of EICO and SCM are summarized.

The calculated contour plots of axial velocity and turbulence kinetic energy (TKE) from the second test condition are shown in Fig. 6. They represent the sectional (xy-plane) views at several z locations. The z locations are selected from where the y-axis (vertical) coincides with the three injector-element centers of different columns of the 9-element injector array: the right (-0.0254), the middle (0.0), & the left (0.0254). The magnitude of mean velocity ranges from -5 to 55 m/s. The flow-field is mainly characterized by nine swirl-induced primary recirculation zones formed behind each one of the injector elements. The shape and size of all recirculation zones of both fueled and non-fueled elements appear to be similar. The recirculation length is roughly about one diameter of the venturi exit (= 22.5mm). The maximum velocity is found to occur near the throat of the venturi.

The simulation captures the sharp gradients that exist in the shear layers formed downstream of the venturi exit plane. This is evident from the TKE contours observed particularly in this region of the non-fueled elements. However, the high levels of TKE formed in this region dissipate quickly downstream of the dump plane. The TKE trends are in agreement with both the non-reacting single single-swirler experimental data of [16] and the predicted non-reacting results of 9-element configuration of [2]. However, it is noteworthy that the maximum levels of both axial velocity and TKE reported in [2] are much higher than those observed in our current calculations. It is because under normal engine operating conditions, the inflow air mass flow rates are about 2.5 times higher. The poor mixing resulting from the decreased TKE levels is partly responsible for the resulting emissions. Also, in this region the TKE levels associated with the fueled (reacting) elements are much lower than the non-fueled. This is consistent with the differences observed between reacting and non-reacting calculations in other studies [2].

Fig. 7 provides some sectional views & a 3D perspective view of the spray particle distribution. A majority of spray droplets vaporize within a short distance of 13mm from the venturi exit. However, some vaporization continue to take place farther downstream (57 mm). As expected, most of the droplets vaporize faster behind the fueled injector elements ((see Fig. 8). Behind the non-fueled injectors, the droplet vaporization continues farther downstream. Downstream of the primary flame zone, there appears to be some mixing of droplets originated from different injector elements.

Several sectional views of gas temperature and hydroxyl (OH) mass fraction are shown in Fig. 8. The gas temperature ranges between 500 to 2200 deg. K and the OH mass fraction from 0.0 to 0.005. The temperature contours show the formation a lifted flame downstream of the dump plane. The hydroxyl contours are shown to provide a better understanding of the combustion activity. Most of the combustion seemed to take place in a near-field primary flame zone (as evidenced by the high concentration levels of OH). Based on what we observed in our earlier investigation of spray flames [15], combustion in the primary flame zone is likely to take place in a predominantly premixed flame environment. Further downstream, combustion takes place in a predominantly diffusion flame environment [15]. It is also noteworthy that under normal engine operating conditions most of the combustion takes place within 25 mm of the combustor [2]. In our present calculations, it extends further downstream due to the formation of a locally fuel-rich environment in the central region. The reasons for this behavior could be attributed to the poor mixing resulting from decreased TKE levels.

The contour plots of $jet-a$, O_2, C_2H_4, C_2H_2, SVF (soot volume fraction), & SPD (soot particle diameter) are shown in Fig. 9. They represent the sectional views at $z = 0.0$. The presence of gaseous fuel vapor in the diverging section of venturi is expected based on the spray article distribution observed in Fig. 7. The oxygen levels are consistent with the observed combustion behavior earlier. The early kinetic steps include the breakup of jet-a into several smaller hydrocarbon components such as ethylene. In particular, ethylene plays an important role into the formation of acetylene, the soot precursor. The contour plots of C_2H_4 & C_2H_2 are shown to provide a better understanding into soot formation. The mass fraction of ethylene ranges between 0.0 to 0.12

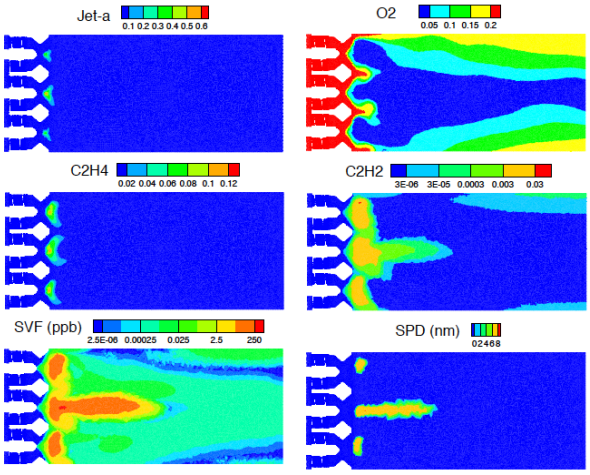

Fig. 9 Sectional views of species mass fractions, SVF & SPD at z = 0.0 (FAR = 0.024 & T_3 = 569 deg. K).

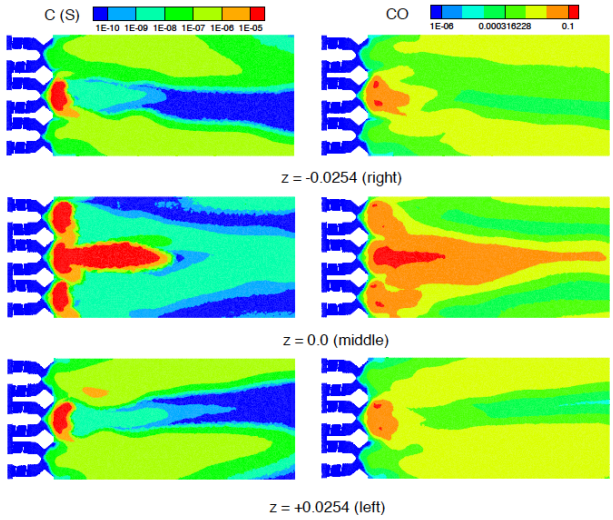

Fig. 10 Sectional views of soot and CO mass fractions (FAR = 0.024 & T_3 = 569 deg. K).

& acetylene from 0.0 to 0.03. The soot nucleation and growth rates are dependent on the concentration levels of acetylene. As anticipated followed by the jet-a breakup, ethylene appears first followed by acetylene downstream. The SVF ranges between 0.0 to 250 (ppb), and SPD from & 0.0 to 8.0 (nm). The location of the maximum levels of SVF becomes more evident after looking at the concentration levels of acetylene in the corresponding region. In the central region behind the pilot injector, the soot accumulation continues further downstream. However, behind the main injector elements it gets oxidized faster due to increased availability of oxygen from the mixing of air from the surrounding non-fueled injector elements. Conversely, lack of oxygen leads to the formation of more soot in the central region. It is important to note that the SVF levels continue to decline further downstream. At exit boundary, the SVF levels range between 0.0 to 0.025.

The contour plots of soot and CO mass fractions at different z locations are shown in Fig. 10. The soot mass fraction varies from 0.0 to 1.0e-05 and CO from 0.0 to 0.1. The behavior of both C(S) and CO is mostly similar. The C(S) behavior at $z = 0.0$ is similar to what we discussed earlier with respect to SVF. However, its behavior is quite different at the other two z locations where only one main (middle) injector is fueled. At the side-column injector elements, a high soot region is formed in the close proximity behind the main fueled-injector. Further downstream in the central region, negligible amount of soot is observed. It is because soot oxidation is further aided by the increase in the availability of oxygen from the non-fueled injectors, and by the high levels of gas temperature observed in this region. However, in the region behind the non-fueled injectors, the soot spreading extends all the way to the exit boundary. The reasons for this behavior could be attributed to reduced soot oxidation resulting from low levels of both temperature and soot mass fraction, & smaller soot particle sizes observed in this region.

For comparisons sake, the contour plots of some selected variables obtained from different calculations (at z = 0.0) are shown in Figs. 11-14. The axial velocity and temperature results are shown in Fig. 11. As expected, the flow and thermal properties are mostly similar since the test conditions are drawn from a narrow range of engine operating conditions. In order to gain some understanding of the differences observed in the behavior of CO & soot emissions, the contour plots of OH and C_2H_2 are shown in Fig. 12, $C(S)$

Table 2. EICO & SMC comparisons at the exit plane.

Calculations	(1)	(2)	(3)
Measured EICO	71.8	45.8	15.1
Predicted EICO	73.25	69.20	101.58
Measured SMC (mg/m^3)	0.0725	0.020	0.0365
Predicted SMC (mg/m^3)	0.05983	0.0423	0.0189

and CO in Fig. 13, & SVF & SPD in Fig. 14. Although the behavior of both OH and C_2H_2 is mostly similar in the first two test conditions, an increase in T_3 (from 525 to 569 deg. K) leads to slightly better combustion as evidenced by the increase in OH levels in the primary reaction zone. However, an increase in the F/A ratio from 0.024 to 0.028 leads to a significant change in the region of combustion activity. Particularly in the central region, there is a significant shift in the primary reaction zone. Also, the spreading of acetylene continues farther downstream in the central region. The reasons for this behavior could be attributed to the formation of a fuel-rich environment in the central region behind the pilot injector. The contour plots of $C(S)$ and CO are shown in Fig. 13. There is an overall reduction in both soot and CO emissions as a result of improved combustion from increased T_3. In particular, it is more evident in the reduction of high soot region formed in the central region. However, an increase in the F/A ratio leads to a significant downstream shift in the location where the hight soot region is formed in the middle. The observed behavior is consistent based on our earlier discussion involving T, OH and C_2H_2. The contour plots of SVF & SPD are shown in Fig. 14. The expected behavior of both SVF and SPD is consistent following what we observed earlier on C(S).

The comparisons between the experimental and predicted results of $EICO$ and SMC (mg/m^3) are shown in Table 2. The soot calculations are consistent with the experimental behavior showing a reduction in SMC with an increase in either T_3 or F/A ratio. Although there is a good comparison between the predicted and calculated values of $EICO$ in the first two test cases, it differs by a significant measure in the last case.

7. CONCLUDING REMARKS

The OpenNCC was used to investigate the CO and soot emissions generated by a partially-fueled 9-element LDI combustor in the idle engine operating conditions. This work was undertaken based on

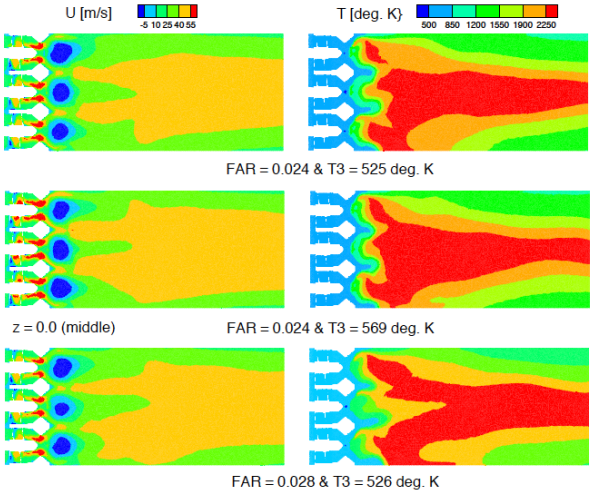

Fig. 11 Contour plots of axial velocity and temperature at different test conditions at z = 0.0.

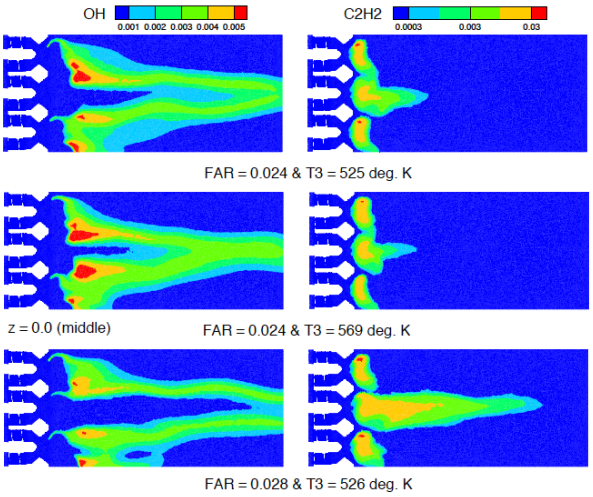

Fig. 12 Contour plots of OH and C2H2 mass fractions at different test conditions at z = 0.0.

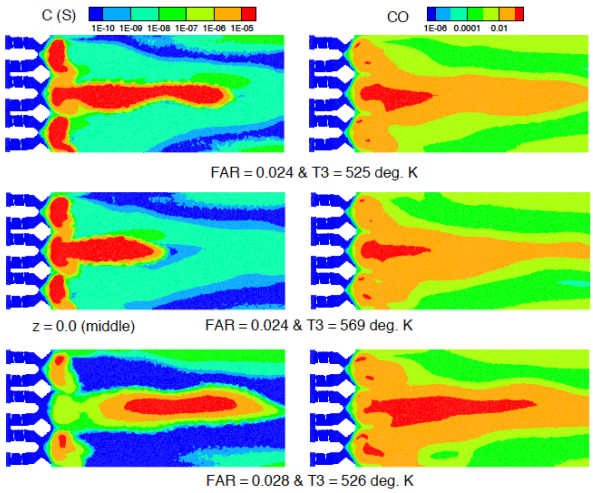

Fig. 13 Contour plots of soot and CO mass fractions at different test conditions at z = 0.0.

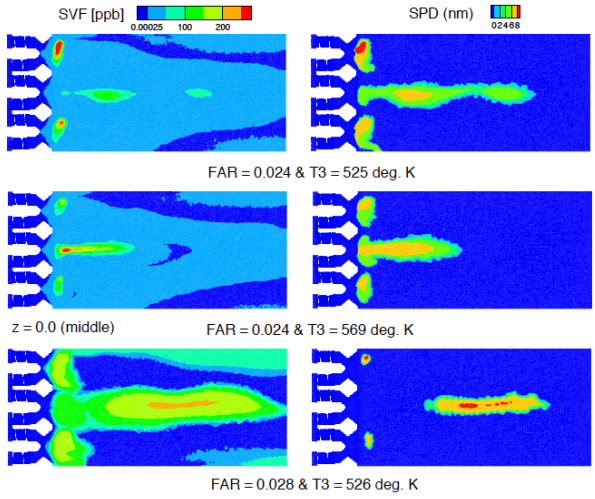

Fig. 14 Contour plots of SVF and SPD at different test conditions at z = 0.0.

the best practices established in the areas of mesh-optimization, spray modeling, ignition and kinetic modeling, and turbulence modeling for LDI computations based on the OpenNCC RANS methodology [2]. Moreover in an effort to extend our current gas-turbine combustor design & testing effort to CO and soot particle emissions, we incorporated the soot models of [11] & [12] and the 62-species jet-a/air skeletal mechanism of [13] into OpenNCC. It is noteworthy that a separate transport equation is solved for all individual species.

We presented the results for three different test conditions selected from the CO & soot particle measurements of [10] based on a testing performed in a combustion rig, CE-5, operated at NASA Glenn research center. The test conditions were chosen to gain some understanding of soot & CO behavior resulting from variations in either T_3 or FAR. The results are summarized as follows:

- Since the test conditions were drawn from a narrow range of the idle engine operating conditions, the calculations showed that the overall behavior was mostly similar in the results obtained for both gas temperature & velocity. However, substantial differences were found in the behavior of soot and CO emissions.

- The calculations helped to identify several reasons behind soot formation in different regions of the combustor. The poor mixing resulting from decreased TKE levels lead to the formation of a fuel-rich environment in the central region. It also lead to increased accumulation & further spreading of the soot downstream of the pilot injector in the central region of the combustor. However, the soot formed behind the main fueled-injector elements oxidizes more rapidly due to increased availability of oxygen from the air supplied by the surrounding non-fueled injector elements. In the region behind the non-fueled injectors, the soot spreads much farther downstream all the way to the exit boundary. It is a result of reduced soot oxidation contributed by several factors: low levels of temperature, C(S), & soot particle sizes observed in this region.

- The predicted results were compared with the reported experimental data on SMC & $EICO$. The experimental results showed that improved combustion resulting from an increase in either T_3 or FAR lead to a reduction in both soot and

CO emissions. The predicted soot & CO results were mostly in similar agreement but in one test condition associated with higher F/A ratio the calculated $EICO$ exceeded by a considerable measure.

The soot & EICO results could be improved by undertaking calculations based on TFNS (Time-Filtered Navier Stokes) solution with LDM (large eddy mixing) or turbulence chemistry interaction with scalar Monte-Carlo PDF [2, 5-7, & 15]. Also, there is a need to incorporate a radiation model in our soot computations.

ACKNOWLEDGMENTS

This work was supported by the NASA's Transformational Tools and Technologies project. The authors would like to thank Dr. Jeff Moder for his help & guidance during the course of this investigation, & for identifying the test conditions used in this study.

REFERENCES

1. Tacina,R., Lee, P., & Wey, C.W., "A Lean-Direct-Injection Combustor Using a 9 Point Swirl-Venturi Fuel Injector," ISABE-2005-1106, 2005.

2. Ajmani, K., Mongia, H., & Lee, P.,"CFD Best Practices to Predict NOX, CO and Lean Blowout For Ccombustor Design", GT2013-95669, Proceedings of ASME Turbo Expo 2013, June 3-7, 2013, San Antonio, Texas, USA.

3. Cai, J., Jeng, S.-M., and Tacina, R., "The Structure of A Swirl-Stabilized Reacting Spray Issued From an Axial Swirler," AIAA Paper 20051424, 43rd AIAA Aerospace Science Meeting and Exhibit, Reno NV.

4. Fu, Y., Jeng, S-M., & Tacina, R., "Characteristics of the Swirling Flow Generated by an Axial Swirler," Proceedings of ASME Turbo Expo 2005, GT2005-68728.

5. Liu, N.-S., Shih, T.-H. and Wey, C.T., Numerical Simulations of Two-Phase Reacting Flow in a Single-Element Lean Direct Injection (LDI) Combustor Using NCC, NASA/TM2011-217031.

6. Liu, N.-S., Shih, T.-H., & Wey, C.T., "Comprehensive Combustion Modeling and Simulation: Recent Progress at NASA Glenn Research Center," ISABE-2007-1268, 18th International Symposium on Air Breathing Engines, Beijing, China, September 2-7, 2007.

7. M.S. Raju, "EUPDF-II - An Eulerian-Based Monte Carlo Probability Density Function (PDF) Solver - User's Manual," NASA/CR-2004-213073, NASA Lewis Research Center, Cleveland, Ohio.

8. Eberle, C., Gerlinger, P., & Aigner, M., "A Comparison of URANS and LES For Soot Predictions in an Aero-Engine Model Combustor," Deutscher Luft- und Raumfahrtkongress 2015, DocumentID: 370050.

9. Raju, M.S., Moder, J.P., & Wey, C.T., "Preliminary Soot Computations Based on a Model Aircraft Combustor With OpenNCC," ISABE-2019-24007, 24th International Symposium on Air Breathing Engines, Canberra, Australia, September 22-27, 2019.

10. Lobo, P., Kettlinger, J., & Podboy, D., "NASA NvPM Test," PMTG MEASURE ahg call, 11 January 2017.

11. Fairweather, M., Jones, W. P., and Lindstedt, R. P., "Predictions of Radiative Transfer from a Turbulent Reacting Jet in a Cross-Wind", Combustion & Flame, Vol. 89, 1992, pp. 45-63.

12. Liu, Fengshan, Guo, Hongsheng, Smallwood, Gregory J, & Gulder, Omer, "Numerical modeling of soot formation and oxidation in laminar coflow non-smoking and smoking ethylene diffusion flames," Combustion Theory and Modeling, vol. 7, no. 2, pp. 301-315 (2003).

13. Lu, T., & Law, C.K., Proc. Combt. Inst., 30: 1333-1341, (2005).

14. Raju, M.S., "LSPRAY-V: A Lagrangian Spray Module," NASA/CR-2015-218918, NASA Glenn Research Center, Cleveland, Ohio, November, 2015.

15. M.S. Raju, "On the Importance of Chemistry/Turbulence Interactions in Spray Computations, Numerical Heat Transfer, Part B: Fundamentals", No. 5, Vol. 41, pp. 409-432, 2002.

16. Fu, Y., Aerodynamics and Combustion of Axial Swirlers, Ph.D. Dissertation, University of Cincinnati, 2008.